SINTEF

Investigating simplified modeling choices for numerical simulation of CO2 storage with thermal effects

Odd Andersen, Halvor M. Nilsen

Investigating simplified modeling choices for numerical simulation of CO_2 storage with thermal effects

Odd Andersen[a,*], Halvor M. Nilsen[a]

[a]*SINTEF Digital, Mathematics and Cybernetics, PB 124 Blindern, 0314 Oslo, Norway*

Abstract

Temperature is a key variable for the modeling of geological CO_2 storage, and any simulation model must take it explicitly or implicitly into account. In the most basic case, the assumption of reservoir temperature is simply reflected in the particular choice of fluid properties. More advanced models represent temperature as an imposed field that vary with spatial coordinates but remains unchanged in time. Yet more advanced models include thermal fields that evolve in time, obtained from explicit modeling of heat transport based on energy conservation.

When modeling geological CO_2 storage at large spatial and temporal scales, it is beneficial to employ simplified flow models with significantly lower computational requirements than fully resolved 3D simulations. At the large spatial scales and low flow rates associated with CO_2 migration studies, temperature can be reasonably considered as an imposed external field dictated by the geothermal gradient, with CO_2 and brine assumed to be in thermal equilibrium with the surrounding rock. Closer to an injection well, the picture is different. CO_2 may be injected at a temperature significantly different from that of the aquifer, which leads to an expanding thermal front around the injection well. This local change in temperature not only affects fluid properties, but also geomechanical stresses and the rate of geochemical reactions. For these reasons, an adequate model of temperature evolution should be included in the simulation model.

In this article, we examine whether certain simplified approaches used to simulate CO_2 storage at the large scale may be adapted and applied to model the regions affected by the thermal front. We do this by comparing the results from upscaled (vertically integrated) flow models extended with heat transport and different choices of overburden representations against highly resolved 3D models. These comparisons are carried out for a number of test cases spanning a wide range of scenarios constructed to minimize or maximize specific characteristics of the coupled flow-thermal system, namely the Peclet number, the gravity number and the amount of thermal bleed.

Our results suggest that the thermal front can be reasonably modeled in many practical cases using a vertically integrated flow model with constant vertical temperature. The results also suggest that a simplified overburden representation can often be adequate, particularly for scenarios with low thermal bleed, although there will be some amount of overestimation on the advancement of the thermal front and distortion of the thermal front shape. We also argue that the impapct of a simplified overburden representation is very similar to the use of linear heat transfer coefficients. On the other hand, while models that completely neglect thermal bleed may perform acceptably in some low-bleed settings, they can lead to very large errors in other cases.

Keywords: CO_2 storage, thermal modeling, vertical-equilibrium models, reservoir simulation

1. Introduction

1.1. The role of temperature in CO_2 storage modeling

Any model for simulation of geological CO_2 storage must make some assumption on temperature, which has a first-order impact on CO_2 density and viscosity, thus also on fluid flow. Failure to properly represent the temperature of a storage formation can significantly distort the results. For instance, uncertainty about the actual temperature conditions at the Sleipner storage site in the Norwegian North Sea has led to large variations in the estimated CO_2 mass associated with evolving CO_2 layers that have been tracked by time-lapse seismic over the past couple of decades [1, 2]. Likewise, the amount of gravity fingering occurring as the CO_2 migrates in the aquifer is dictated by the CO_2 mobility, which is significantly affected by temperature and thus potentially sensitive to the temperature model or assumption.

---

*Corresponding author.
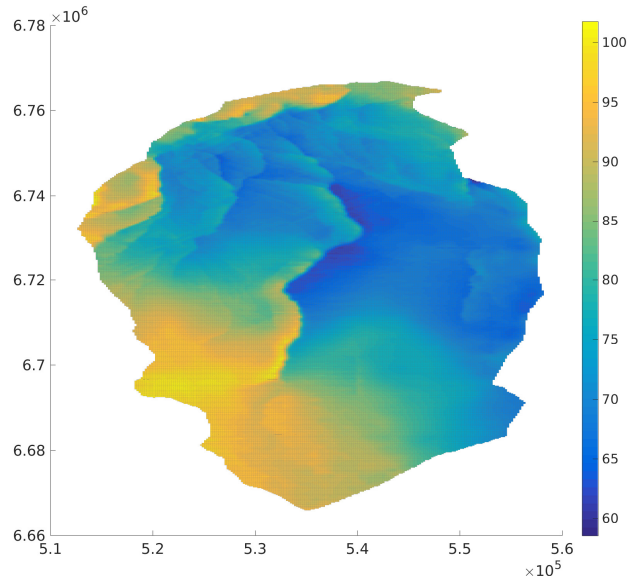Email addresses:* odd.andersen@sintef.no (Odd Andersen), HalvorMoll.Nilsen@sintef.no (Halvor M. Nilsen)

Figure 1: Caprock temperature for the Johansen formation, assuming a thermal gradient of 30°C per kilometer depth, and sea floor temperature of 7°C. Color represents temperature in °C. Lateral coordinates are expressed in meters. The lateral extent covered by the formation model is thus approximately 45 km east-west and 50 km north-south. The figure was generated using the `exploreCapacity` interactive script provided in [8].

When modeling CO_2 storage at the large (aquifer) scale, it is usually sufficient to consider temperature as an externally imposed field, determined by the local thermal gradient. This treatment can be justified by the observation that CO_2 temperature equilibrates with that of the surrounding rock at a relatively short distance from the injection well. After this happens, only a limited number of physical effects will have the ability to significantly change CO_2 temperature. CO_2 can migrate into regions with lower temperature, undergo temperature changes as a result of rapid expansion or compression, of brine vaporization into CO_2, of CO_2 dissolution into brine, or as a result of other geochemical reactions [3]. Away from the local region around the injection well, neither of these mechanisms are expected to be rapid enough or large enough to cause a significant temperature difference between CO_2 and the surrounding rock, thus justifying the use of a fixed, externally imposed temperature field in the simulation [4]. Figure 1 displays such an imposed thermal field for the Johansen formation [5, 6], under the assumption of a thermal gradient of 30° per km.

For storage operations, CO_2 is typically injected into a geological formation at a temperature substantially different from that of the ambient conditions. It has for instance been argued that the injection of 'cold' CO_2 is desirable from an economic point of view [7]. This leads to a distinct and expanding thermal front around the injection well, as the surrounding rock thermally equilibrates with the temperature of the injected fluid. A conceptual illustration is shown in figure 2. At some point beyond this front (which may be more or less sharp), CO_2 will have completely acquired the temperature of the aquifer, and explicit thermal modeling is no longer required. Due to the significant heat capacity of rock, the advancement of the thermal front will be relatively slow compared to the flow of CO_2 itself. Because of the inverted-cone shape of the CO_2 front, it is nevertheless possible that the thermal front intersects with the CO_2/brine interface. Heat is not solely transported by advection with fluid flow in the aquifer, but also through conduction, both in the aquifer itself and in the over- and underburden. this exchange of heat with the aquifer surroundings is referred to as *thermal bleed*, and affects the speed and shape of the thermal front.

There are multiple reasons to model the thermal development around an injection well. Temperature has a first-order effect on fluid properties such as density and viscosity, as well as other processes that may affect flow such as salt precipitation [9] and rates of geochemical reactions [10]. In addition, thermal expansion/contraction of the rock itself can induce thermal stresses, which need to be understood in order to evaluate the potential for mechanical damage [11]. Analyzing the interplay between fluid flow, thermal developments, geochemistry and/or geomechanics requires coupled numerical simulations that can be highly computationally demanding. There is thus an interest in reducing computational requirements by using the simplest possible models that still provide adequate results. In the present paper, we explore the potential for using simplified models to represent thermal developments, assessing the impact various simplifying assumptions have on the thermal front for a range of different scenarios.
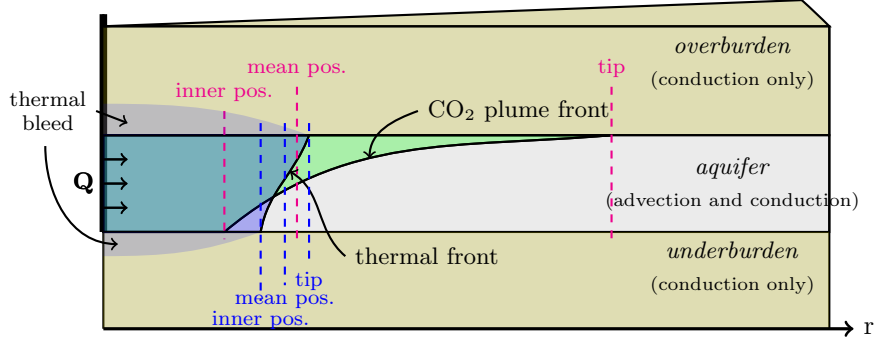
Figure 2: Conceptual, radial model of CO_2 and heat transport in the region surrounding an injection well situated in a flat, horizontal aquifer. **Q** here represents the (fixed) injection rate.

1.2. Previous related work

Studies related to heat transport from fluid injection into an aquifer date back to at least the 1950s. An early analytic solution for the one-phase, one-dimensional injection case with thermal bleed was proposed in [12]. This solution has later been generalized and extended in various ways, such as the inclusion of thermal conduction in the aquifer [13], thermal dispersion, and axi-symmetric geometry [14]. Analytic approximations for multi-phase flow with simplified physics have also been developed; a good overview can be found in the introduction of [15], which also presents a semi-analytic two-phase model that includes the effect of thermal bleed. Analytic approximations of one-phase, one-way coupled thermal-hydro-mechanical fluid injections have also been developed, e.g. [16], [17]. Analytical and semi-analytical solutions to the thermal problem are attractive in many ways, as they provide rapid solutions and theoretical insight. They are however limited by having to rely on simplifying assumptions that are in general only valid under certain conditions and time-spans. For instance, the model in [15] requires fluids to have constant density, zero lateral heat conductivity, and no gravity segregation, all of which are likely to play an important role in many plausible CO_2 storage scenarios.

In the field of numerical reservoir simulation, [18] employs a flow/thermal/geomechanical model for studying reservoir compaction. An overview of non-isothermal processes associated with CO_2 injection scenarios was presented in [3]. The paper discusses Joule-Thompson expansion, water vaporization, CO_2 dissolution and geochemical reactions, but does not consider thermal bleed into the overburden; all accompanying simulations are carried out under adiabatic conditions. In the studies presented in the paper, the impact of these non-isothermal processes were shown to be limited to a region of about half a kilometer around the injection well, and were relatively small (on the order of $1°C$ or less), especially when considering the potentially large temperature differential between injected CO_2 and resident brine. Specific case studies on the thermo-poromechanical effects of CO_2 storage have also been presented, including [19] for the In Salah storage site in Algeria, and [20] for the FutureGen 2.0 site in the US. The advantages of injecting 'cold' CO_2 was argued in [7], and the associated geomechanical impacts investigated in [11]. A comprehensive article on thermal effects of CO_2 storage is provided in [21].

1.3. Simplified models, CO_2 storage and thermal modeling

Dimensionally reduced flow models based on the assumption of vertical equilibrium (VE) and phase segregation have proved to be very efficient in modeling CO_2 storage at the large scale [22]. Attractive features include significantly reduced computational requirements and sometimes higher vertical precision and better nonlinear convergence properties than their 3D counterparts, as demonstrated in e.g. [23]. An open-source implementation of VE models for CO_2 storage modeling is provided in [8], and is employed to demonstrate their usefulness on real aquifer models in [24, 25, 4]. In these studies, temperature was taken into account as an imposed background field affecting local fluid properties.

The first vertical equilibrium for CO_2 storage that includes energy conservation was presented in [26]. The model consider lateral energy transport to be limited to the CO_2 zone, whose vertical temperature profile is constant. While the overburden is not explicitly represented, heat bleed is modeled using a constant transfer coefficient.

For the purposes of the present paper, we have implemented two similar VE models that include an explicit representation of the over- and underburden (cf. Section 2.1). We compare results with those from full 3D modeling to assess to which extent such VE-models can be usefully employed to model thermal developments caused by injection of CO_2 with different temperature than the surroundings.

3

2. Simplified thermal modeling

As mentioned in the introduction, at the large scale it is usually admissible to consider temperature as an imposed and unchanging background field, defined by the geothermal gradient. Moreover, the assumption of vertical equilibrium allows the use of dimensionally reduced (i.e. vertically integrated) flow models for computational efficiency. Since the top and bottom boundaries of the aquifer are frequently considered impervious to fluid flow, and since transport of heat is not included in the flow model, there is no need for an explicit representation of the over/underburden at this scale.

In regions where heat transport plays a significant role, flow models must be extended to include conservation of energy. For dimensionally reduced models, the inclusion of energy conservation requires making assumptions on the vertical temperature profile within the aquifer. Moreover, if thermal bleed is to be taken into account, additional assumptions must be made. On one hand, the flow model may be embedded within a larger domain for heat convection that includes a fully resolved grid of the surrounding rock. On the other hand, heat flow into the surrounding rock could be modeled with a lower resolution grid, as a constant parameter, or neglected altogether.

This section present the modeling choices that have been considered in the present study. In the following section, results from testing these models on a range of simulation scenarios are presented and discussed. The modeling choices considered are two simple approaches for extending dimensionally reduced flow models with heat transport (Section 2.1), and three choices for the surrounding rock (Section 2.2).

2.1. Vertical equilibrium models with conservation of energy

The fine-scale equations for Darcy-type immiscible two-phase fluid flow in a porous medium are written:

$$\partial_t(\phi\rho_\alpha s_\alpha) + \nabla \cdot (\rho_\alpha \mathbf{q}_\alpha) = \psi_\alpha \qquad \text{(continuity)} \qquad (1)$$

$$\mathbf{q}_\alpha = -\frac{k_\alpha(s_\alpha)}{\mu_\alpha}k(\nabla p_\alpha - \rho_\alpha g\mathbf{e}_z). \qquad \text{(Darcy)} \qquad (2)$$

For each phase α ('n' for CO_2 or 'w' or brine), ρ_α denotes phase density, s_α phase saturation, $\mathbf{q}_\alpha$ phase volumetric flux, k_α relative permeability, μ_α phase viscosity, p_α phase pressure and ψ_α a source term. Moreover, ϕ represents porosity, k intrinsic permeability, g the gravitational constant and $\mathbf{e}_z$ the unitary vector along the z-axis (oriented downwards).

In addition, the conservation equation for energy that includes advective transport, thermal diffusion and pressure work can be written:

$$\partial_t \left(\phi \sum_\alpha s_\alpha \rho_\alpha e_\alpha + (1-\phi)\rho_r e_r \right) + \nabla \cdot \left(\sum_\alpha \rho_\alpha h_\alpha \mathbf{q}_\alpha \right) - \nabla \cdot \lambda\nabla\tau = q_e. \qquad (3)$$

Temperature is represented with the symbol τ, and appears explicitly in the third (diffusion) term, where λ represents effective thermal conductivity. Specific internal energies for phase α and for rock are written e_α and e_r, respectively. We here consider e_r to be a function of temperature only, whereas the e_α are functions of pressure and temperature, as dictated by the corresponding fluid's equation of state (EOS). Rock density is written ρ_r. In addition, h_α denotes specific phase enthalpy, with $h_\alpha(p,\tau) = e_\alpha(p,\tau) + \frac{p}{\rho_\alpha(p,\tau)}$. Finally, q_e denotes the heat source or sink term.

We limit ourselves to the modeling of an immiscible system, which means that energy transfer associated with phase mixing is not captured. Moreover, we only consider situations with no phase change. The Joule-Thompson effect is implicitly captured through the use of fluid properties (ρ_α, e_α and h_α) derived from a full EOS.

Using the assumption of vertical equilibrium in the aquifer, analytical expressions of vertical saturation and pressure profiles can be defined, allowing us to integrate equations (1) and (2) along the vertical direction, thereby defining a new set of upscaled equations defined on a 2D lateral domain. Details on the integration process can be found in previously published literature, e.g. [22, 27, 28]. In this paper, we use the additional simplifying (but not strictly required) assumptions of incompressible rock, vertically constant density, permeability and porosity, zero residual saturation and negligible capillary pressure. For a caprock impervious to fluid flow, the vertically integrated equations become:

$$\Phi\partial_t(\rho_\alpha S_\alpha) + \nabla_{||} \cdot (\rho_\alpha \mathbf{Q}_\alpha) = \Psi_\alpha \qquad (4)$$

$$\mathbf{Q}_\alpha = \frac{S_\alpha}{\mu_\alpha}K(\nabla_{||}P_\alpha - \rho_\alpha g\nabla_{||}\zeta_{\text{top}}). \qquad (5)$$
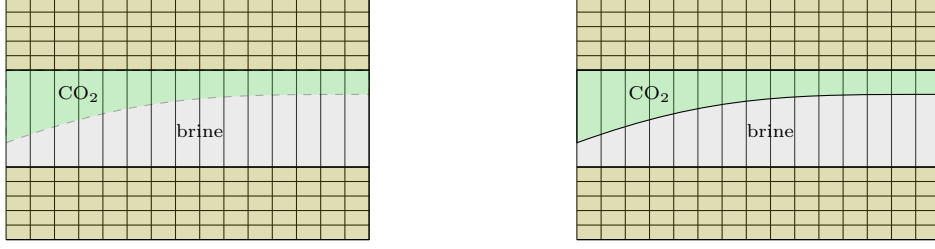
Figure 3: Simulation grids used to compute heat flow for the models VE1 and VE2. For VE1 (left), temperature is considered to be constant in the vertical direction, and represented as a single cell across the vertical extent of the aquifer. For VE2 (right), there are separate temperatures for CO_2 and brine. The simulation grid within the aquifer zone thus consists two cells per vertical column, where the position of the interface between the two cells evolve in time along with the shape and extent of the CO_2 zone.

Upper-case symbols here represent upscaled quantities: vertically integrated porosity and permeability are written Φ and K, vertically integrated phase flux is denoted $\mathbf{Q}_\alpha$ and vertically averaged phase saturations S_α. Upscaled phase pressures P_α are defined as the fine-scale phase pressures taken at the caprock level. The 2D del operator is written $\nabla_{||}$, and ζ_{top} denotes the caprock depth as a function of the lateral coordinates. Similar to the fine-scale equations, there are relationships between upscaled phase saturations and pressures (H representing local aquifer thickness):

$$S_n + S_w = 1 \qquad \text{(saturations sum to one)} \tag{6}$$

$$P_n - P_w = (\rho_n - \rho_w)gS_n H \qquad \text{(upscaled capillary pressure)} \tag{7}$$

In our numerical simulator [8], the equations are discretized using a finite-volume scheme, using two-point flux approximation (TPFA) to compute phase fluxes [29], and solved using a fully implicit Euler time-stepping scheme.

In order to include a similarly upscaled version of the energy conservation equation (3), an assumption must be made on the vertical thermal profile. The simplest is to assume a constant vertical temperature profile within the aquifer:

$$\partial_t \left(\Phi \sum_\alpha S_\alpha \rho_\alpha e_\alpha + (H - \Phi)e_{\text{rock}} \right) + \nabla_{||} \cdot \left(\sum_\alpha \rho_\alpha h_\alpha \mathbf{Q}_\alpha \right) - \nabla_{||} \cdot \Lambda \nabla_{||} \tau + \beta_T - \beta_B = Q_e \tag{8}$$

The newly introduced symbols here are Λ for vertically integrated effective thermal conductivity, Q_e for the vertically integrated source term, and two new quantities β_T and β_B that represent conductive flux of heat across the top and bottom boundaries, respectively. These terms appear when applying Leibniz' integration rule on the heat diffusion term, and are spelled out:

$$\beta_T = \lambda_{\text{ob}}[\nabla_{||}\tau, \partial_z \tau_{|_{\text{top}}}] \cdot [-\nabla_{||}\zeta_{\text{top}}, 1] \tag{9}$$

$$\beta_B = \lambda_{\text{ob}}[\nabla_{||}\tau, \partial_z \tau_{|_{\text{bot}}}] \cdot [-\nabla_{||}\zeta_{\text{bot}}, 1] \tag{10}$$

Again, ζ_{top} and ζ_{bot} represent the depth of the caprock and aquifer bottom, respectively, and λ_{ob} is the thermal conductivity of the over/underburden. Note that since we have here assumed τ to be vertically constant within the aquifer, the practical values of $\partial_z \tau_{|_{\text{top}}}$ and $\partial_z \tau_{|_{\text{bot}}}$ will depend on our choice of overburden model. Similar to the fluid flow equations, we choose to employ a finite volume scheme with TPFA to compute heat fluxes, where a vertical aquifer column is treated as a single cell in a 3D grid with an overburden that may be highly or lowly resolved (Figure 3, left). We will refer to this model as 'VE1'.

A different choice of assumption for the vertical integration of equation 3 is to consider separate but constant temperatures for CO_2 and brine within each vertical column. Since the vertical equilibrium assumption entails phase separation by gravity, we consider CO_2 and brine to be distributed into separate zones with CO_2 on top and brine on the bottom. Our new assumption on the vertical thermal profile therefore means that we have one temperature in the upper CO_2 zone and a possibly different temperature in the underlying brine zone. We now define separate, vertically integrated, heat conservation equations for the CO_2 and brine phases:

$$\partial_t [S_n(\Phi\rho_n e_n + (H - \Phi)e_r)] + (\omega - \gamma_r)\partial_t S_n + \nabla_{||} \cdot (\rho_n h_n \mathbf{Q}_n) + \beta_T - \beta_I = Q_{e,n} \qquad \text{(CO}_2\text{)} \tag{11}$$

$$\partial_t [S_w(\Phi\rho_w e_w + (H - \Phi)e_r)] + (\omega - \gamma_r)\partial_t S_w + \nabla_{||} \cdot (\rho_w h_w \mathbf{Q}_w) + \beta_I - \beta_B = Q_{e,w} \qquad \text{(brine)} \tag{12}$$

The newly introduced quantities γ_r and ω appear when applying Leibniz' integration rule in the presence of a moving interface, after rearranging the resulting terms. They respectively represent the thermal energy

contained in the rock that crosses the moving interface, and the work done by the expanding zone on the contracting one. Their expressions are:

$$\gamma_r = (H - \Phi)e_r \tag{13}$$

$$\omega = \Phi P \tag{14}$$

The other introduced variable, β_I represents flow of heat by conduction across the CO_2-brine interface. Since we assume constant vertical heat profiles within each zone, there is a thermal discontinuity at the interface, and this term is thus not formally well defined as it depends on the z-derivative at this point. In the discrete setting, we can however model this flow of energy using the finite-volume TPFA scheme, by letting each zone constitute its proper grid-cell within the vertical column (Figure 3, right). With this approach, the grid geometry becomes dynamic and will change from one time step to the next. In practice, though, it is possible to keep the grid geometry fixed and rather dynamically modify the transmissibilities associated with the affected grid cells. We refer to this vertically integrated model as 'VE2'. This approach to modeling heat flow between the two fluid zones means that the aquifer has a vertical discretization of two cells - a fairly coarse approximation. A mathematically correct model of the heat flux across the fluid-fluid interface using the TPFA method would require a fine discretization, with vertical cell thicknesses that tends towards zero. The impact of this coarse, two-cell grid on the heat exchange between fluids is discussed towards the end of Section 4.

2.2. Representing the overburden

There are different ways to model thermal bleed. The simplest is to ignore it and consider thermal processes in the aquifer as adiabatic, which may be permissible at short times and high injection rates [3]. For analytical or semi-analytical solutions, bleed can be approximated using an effective heat loss coefficient [15, 12, 14], which makes heat transfer between aquifer and overburden proportional to local temperature disturbance. For numerical simulations, the aquifer can be embedded in a larger domain that include a certain part of the surrounding rock, allowing for explicit numerical computation of the heat exchange between the aquifer and its surroundings based on the discretized heat transport equations. In this case, the modeler may want to limit the additional domain as much as possible, both in terms of physical extent and of number of discrete grid cells, to limit the additional computational cost.

In this paper, we compare three different representations of the overburden, as illustrated in Figure 4. The first representation uses a grid with high vertical resolution, with cells that become progressively thinner towards the interface with the aquifer itself. Results from this representation will be used as a "benchmark" basis for comparison. The thickness of the over- and underburden domains are based on an analytical estimate for how far the temperature perturbation will ultimately reach into the overburden at the end of simulation (see discussion below). We label this representation 'FINE'. The second representation uses over- and underburden domains with the same thicknesses as 'FINE', but with the lowest possible resolution - a single grid cell in height. As we will see in Section 4, such a grid entails a bleed rate that remains approximately linear over the course of the simulation, thus resembling the use of heat loss coefficients found in analytical models. We will refer to this representation as 'COARSE'. The third approach, which we label 'ADIABATIC', is to consider the aquifer as thermally insulated.

In order to determine the required thickness of the overburden, we can use a simple analytical estimate. The propagation of the thermal perturbation into the overburden will be closest in the region immediately around the well. If we consider heat flow into the overburden in this region to be predominantly along the z-coordinate, the vertical thermal profile will resemble that of the one-dimensional linear diffusion problem with background temperature τ_0 and temperature τ_i imposed at $z = 0$ for time $t > 0$. The solution to this problem is:

$$\frac{\tau - \tau_0}{\tau_i - \tau_0} = \mathrm{erfc}(\frac{z}{2\sqrt{\kappa' t}}) \tag{15}$$

where 'erfc' is the complimentary error function and κ' the effective overburden diffusivity, which relates to the effective thermal conductivity λ', density ρ' and specific heat capacity c' of the overburden as $\kappa' = \frac{\lambda'}{\rho' c'}$ We here refer to the denominator $2\sqrt{\kappa' t}$ in the argument on the right side of Equation 15 as the conduction length scale, and give it the name L_c. The complimentary error function decays rapidly away from zero. At $z = 2L_c$, the temperature disturbance is less than 0.5 percent of $\tau_i - \tau_0$. A model of the overburden with vertical thickness $2L_c$ will thus be practically sufficient to correctly capture the thermal bleed occurring within the specified time-frame. It should be noted that this estimate is conservative - at early times or for low injection rates, the heat flow around the injection point will be more spherical than linear, thus reducing vertical reach into the overburden [30].
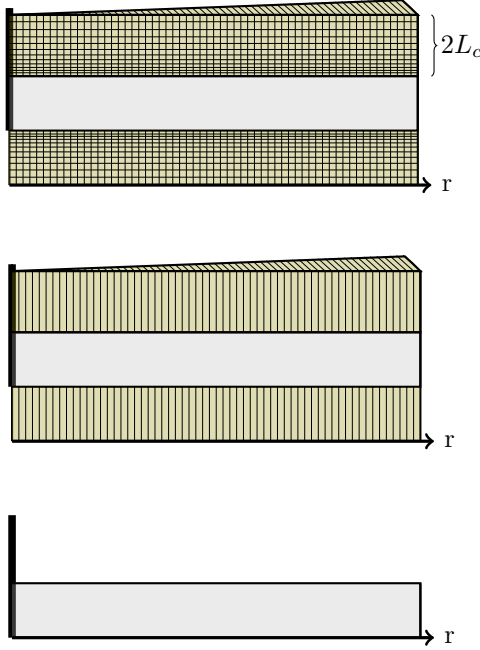
6

Figure 4: Different grid models of the over- and underburden around an injection site. *Top picture*: Highly resolved grid in the vertical direction, discretization progressively finer towards aquifer boundary; *Middle picture*: Lowest possible vertical resolution - a single cell covers the entire thickness of the overburden (and similar for the underburden); *Bottom picture*: No representation of the over- and underburden - aquifer treated as thermally insulated.

2.3. Possible thermal conditions for CO_2 injection scenarios

The purpose of Section 3 is to test the models discussed above on a wide range of injection scenarios that can be defined using parameter values that are within reasonable bounds for CO_2 storage. We will limit ourselves to scenarios that involve a constant injection rate. We characterize the injection scenarios in terms of three dimensionless numbers: the thermal Peclet number, the amount of thermal bleed ("thermal bleed number") and the gravity number, as discussed below. Since these numbers by themselves are not sufficient to capture all relevant aspects of two-phase flow (e.g. mobility ratio), we also make a distinction between a 'cold' injection case (injection of CO_2 at 5°C) and a 'hot' injection case (injection of CO_2 at 70°C). In the following discussion, we use subscripts f to refer to fluid properties and e to refer to effective properties of the fluid-saturated porous medium (porosity-weighted averages of rock and fluid properties). Properties marked with an apostrophe (') refer to the overburden, otherwise they refer to the aquifer.

The Peclet number for heat transport expresses the ratio between advection and conduction in the aquifer. for the axi-symmetric injection case, it can be defined as [14]:

$$Pe = \frac{Q_{\text{inj}}R}{4\pi\phi H\kappa} \tag{16}$$

where $\kappa = \lambda_e/\rho_e c_e$ is the effective diffusion coefficient of the aquifer and $R = \phi\frac{\rho_f c_f}{\rho_e c_e}$. Since we use a full equation of state to derive fluid properties, the specific heat capacity c_f is computed as $c_f = \partial_\tau h(p,\tau)$, where h denotes the enthalpy function. The velocity v of the heat front relates to the volumetric injection rate Q_{inj} and the distance r from the injection well according to $v = \frac{Q_{\text{inj}}}{2\pi r H}\frac{\rho_f c_f}{\rho_e c_e}$, so we also have that $Pe = \frac{vr}{2\kappa}$. A third and equivalent formulation is: $Pe = \frac{Q_{\text{inj}}\rho_f c_f}{4\pi H\lambda_e}$. Note that Pe here neither depends on time nor distance from well.

The thermal bleed number Bl describes the ratio between conduction in the overburden and convection in the aquifer [14]. In the radial case, it can be expressed as:

$$Bl = \frac{\xi}{H}\sqrt{t\kappa'}, \qquad \text{with: } \xi = \frac{\rho' c'}{\rho_e c_e} \tag{17}$$

As can be seen from formula (17), the thermal bleed number is time-dependent.

The gravity number is a dimensionless group defined for two-phase flow and represents the ratio of buoyant to hydrodynamic and viscous forces [22]. It affects the evolution of the CO_2 plume shape, thereby also the heat transport. For uniform rock parameters, it can be expressed as:

$$\Gamma = \frac{2\pi k\Delta\rho g H^2}{\mu_w Q_{\text{inj}}} \tag{18}$$

Table 1: Simulation parameters that influence the Peclet, Bleed and Gravity numbers. Reasonable ranges for CO_2 storage scenarios are suggested in the middle column, whereas the last column indicates the impact on Pe, Bl and Γ. A '+' sign indicates that the dimensionless number is an increasing function of the given parameter, a '-' sign that it is a decreasing function, and 'o' indicates a non-monotonous relationship.

parameter		min.	max.	unit	Pe	Bl	Γ
porosity	ϕ	0.1	0.36	-		o	
permeability	k	0.013	5	D			+
aquifer thickness	H	10	200	m	−	−	+
aquifer thermal conductivity	λ	1.2	6.4	W/(m K)	−		
overburden thermal conductivity	λ'	1.2	6.4	W/(m K)		+	
aquifer rock density	ρ	2500	2800	kg/m^3		−	
overburden rock density	ρ'	2500	2800	kg/m^3		+	
aquifer heat capacity	c	640	900	J/(kg K)		−	
overburden heat capacity	c'	640	900	J/(kg K)		+	
aquifer depth	d	1000	3000	m	−[1]	o	+
thermal gradient	$\partial_z\tau_0$	25	50	°C/km		o	o
injection temperature	τ_i	20	70	°C	o	o	−
mass injection rate	$\rho_n Q_{\text{inj}}$	0.1	20	megatonnes/year	+		−
duration of injection	t	1	20	years		+	

Table 2: Dependence of Pe, Bl and Γ on fluid properties, and whether they have been evaluated using injection or reservoir temperature and pressure. 'inj' indicates fluid properties evaluated at (estimated) injection pressure and temperature; 'res' indicates that fluid properties evaluated at reservoir conditions have been used. The three last columns indicate the change in the specific fluid property value as a function of temperature, pressure and depth, within the minimum and maximum limits (same legend as in Table 1). See also Table 3.

	Pe	Bl	Γ	change with τ	change with p	change with depth
μ_w			res.	−	+	−
μ_n	inj.			o	+	+
ρ_w			res.	−	+	−
ρ_n	inj.		inj./res.	−	+	+
$\Delta\rho$			res.	o	−	−
$(\rho c)_n$	inj.	inj.		−	o	o
λ_n	inj.			o	+	+

where μ_w is brine viscosity and $\Delta\rho$ the density difference between the two phases (gas and brine).

The ranges of values that can be taken by Pe, Bl and Γ in the context of CO_2 storage scenarios are obviously dictated by the ranges of realistic values of the parameters that go into the parameters that go into their definition. Some of these parameters are also linked: fluid densities and viscosities are dictated by temperature and pressure, which again depend on aquifer depth and thermal gradient. It is also clear that the values of Pe, Bl and Γ are linked by dependence on common simulation parameters, so that they cannot all achieve their maximum or minimum values simultaneously. The dependence of these numbers on simulation parameters is listed in Table 1, which also suggests reasonable upper and lower limits on the values of each parameter. Some of these dependencies are subtle. For instance, the value of Bl depends on the injection rate, since higher rates leads to higher injection pressures, which again affects the fluid properties used to compute the effective properties ρ_e and c_e of the medium. In the following section, we examine the performance of simplified models on the scenarios associated with extremal values of Pe, Bl and Γ, under the assumption that the impact of the model choice will be similar but less pronounced for intermediate values of these dimensionless numbers.

To represent the full range of possibilities, we aim to test our simulation models on the scenarios associated with maximal or minimal values of Pe, Bl and Γ, for injection of either 'hot' or 'cold' CO_2. In most cases, the dependence of Pe, Bl or Γ on a given simulation parameter is monotonous, meaning that the extremal value of each dimensionless number is found at one end of that parameter's range (c.f. right column of Table 1). However, since fluid properties are not linear, the relationships can sometimes be more complex. Although this may imply the existence of local maxima of Pe and Bl at the interior of the specified parameter ranges, we

---

[1] Generally decreasing with depth, but for high injection temperatures and low injection rates, slight non-monotonous behavior was observed.

Table 3: Extremal values for reservoir conditions (τ and p) obtainable using simulation parameters within the ranges presented in Table 1. Fluid properties corresponding to these conditions are also listed. Temperature τ is computed assuming a surface temperature of 10°C, whereas pressure is assumed hydrostatic, using a water density of 1000 kg/m³ in the overburden and a surface pressure of 1 atm.

	(MPa)	(°C)	(kg/m³)		(Pa·s)		(J/kgK)	
Scenario	p	τ	ρ_n	ρ_w	μ_n	μ_w	c_n	c_w
coldest	9.90	35	708	998	5.7×10^{-5}	7.2×10^{-4}	4067	4154
hottest	29.50	160	460	923	3.8×10^{-5}	1.8×10^{-4}	1717	4244

Table 4: Parameter combinations associated with maximum and minimum values of Pe considering a 'cold' injection scenario (20°C). Parameters that do not impact Pe have been chosen to maximize or minimize Bl, as a secondary consideration. Corresponding Pe and Bl numbers for the 'hot' injection scenario (70°C) are listed in parentheses.

	Maximum Pe		Minimum Pe	
	Cold (hot) injection		Cold (hot) injection	
	$Pe = 13765$ (20500)		$Pe = 0.416$ (0.446)	
	$Bl = 5.78$ (6.08)	$Bl = 0.333$ (0.346)	$Bl = 0.310$ (0.315)	$Bl = 0.0492$ (0.0498)
ϕ [-]	0.36		0.1	
k [Darcy]	5		0.013	
H [m]	10		200	
λ [W /(m K)]	1.2		6.4	
λ' [W /(m K)]	6.4	1.2	6.4	1.2
ρ [kg/m³]	2500	2800	2500	2800
ρ' [kg/m³]	2800	2500	2800	2500
c [J/(kg K)]	640	900	640	900
c' [J/(kg K)]	900	640	900	640
d [m]	1000		3000	
$\partial_z \tau_0$ [°C/km]	50		50	
τ_i [°C]	20 (70)		20 (70)	
$\rho_n Q_{\mathrm{inj}}$ [MT/yr]	20		0.1	
t [year]	20	1	20	9.7

limit ourselves to consider the values at the parameter endpoints, assuming that the practical impact of these nonlinearities on the dimensionless numbers is not very strong. It should however be noted that the injection rates specified in Table 1 will sometimes lead to excessive pressure buildup pressure depending on the choice of other parameters. When searching for the parameter combinations that yield the highest and lowest values of Pe, Bl and Γ, injection rates are therefore adjusted downwards whenever the associated injection pressure is estimated to exceed 90 percent of the weight of the overburden. In order to estimate this injection pressure, we use the formula developed by [31], using a 10 cm wellbore radius.

Since we are assessing the performance of VE-models, we also estimate the time required for vertical phase segregation, t^*, for each case. Whenever the duration of a given scenario is less than t^*, we adjust it upwards to avoid situations for which the VE assumption is not expected to hold. Scenarios where t^* exceeds our chosen maximum limit (20 years) are eliminated from consideration. Vertical segregation time has been discussed in previous literature [32, 33]. In line with [32], we here assume VE to be approximately valid for times larger than:

$$t^* = \frac{\phi H \mu_w}{k_{r,\mathrm{loc}} k \Delta \rho g},\qquad(19)$$

where $k_{r,\mathrm{loc}}$ is the relative permeability of the brine phase at some cutoff saturation point. We here set $k_{r,\mathrm{loc}} = 0.2$, which with a simple quadratic Corey-type relperm curve (used in the reference-case simulations) corresponds to a brine saturation of $\sqrt{0.2} \approx 0.45$.

Yet another consideration is whether to use injection or ambient values of pressure and temperature when computing Pe, Bl and Γ. Our choices are presented in Table 2.

The task of identifying the parameter sets corresponding to the extremal values of Pe, Bl and Γ is not completely trivial due to the non-linearity inherent in fluid properties as well as the possibility of having to adjust injection rates down. We have here chosen a brute-force approach where we compute these numbers for all possible parameter combinations, sort them and pick the smallest and largest ones. Since we do this only for the 'cold' injection case, the total number of combinations to search is 8192. The same procedure could have been carried out for the 'hot' injection case, but would in some cases have yielded different parameter combinations, thus making it hard to compare corresponding 'cold' and 'hot' cases. We therefore use the combinations identified for the 'cold' case also when simulating injection of hot CO_2. The resulting parameter combinations are listed in Tables 4–6.

Table 5: Parameter combinations associated with maximum and minimum values of Bl considering a 'cold' injection scenario ($20°$C). Parameters that do not impact Bl have been chosen to maximize or minimize Pe, as a secondary consideration. Corresponding Pe and Bl numbers for the 'hot' injection scenario ($70°$C) are listed in parentheses.

	Maximum Bl		Minimum Bl	
	Cold (hot) injection		Cold (hot) injection	
	$Bl = 6.21$ (6.30)		$Bl = 0.0156$ (0.0168)	
	$Pe = 187$ (184)	$Pe = 35.4$ (34.9)	$Pe = 3.04(2.55)$	$Pe = 0.575(0.480)$
ϕ [-]	0.1		0.1	
k [Darcy]	0.013		5	
H [m]	10		200	
λ [W /(m K)]	1.2	6.4	1.2	6.4
λ' [W /(m K)]	6.4		1.2	
ρ [kg/m^3]	2500		2800	
ρ' [kg/m^3]	2800		2500	
c [J/(kg K)]	640		900	
c' [J/(kg K)]	900		640	
d [m]	3000		1000	
$\partial_z \tau_0$ [°C/km]	25		50	
τ_i [°C]	20 (70)		20 (70)	
$\rho_n Q_{\text{inj}}$ [MT/yr]	0.36		0.1	
t [year]	20		1	

Table 6: Parameter combinations associated with maximum and minimum values of Γ considering a 'cold' injection scenario ($20°$C). Parameters that do not impact Γ have been chosen to maximize or minimize Bl, as a secondary consideration. Corresponding Γ and Bl numbers for the 'hot' injection scenario ($70°$C) are listed in parentheses.

	Maximum Γ		Minimum Γ	
	Cold (hot) injection		Cold (hot) injection	
	$\Gamma = 9840$ (7850)		$\Gamma = 0.00529$ (0.00470)	
	$Bl = 0.310$ (0.315)	$Bl = 0.0159$ (0.0160)	$Bl = 6.21$ (6.30)	$Bl = 0.430$ (0.428)
ϕ [-]	0.1		0.1	
k [Darcy]	5		0.013	
H [m]	200		10	
λ [W /(m K)]	1.2		1.2	
λ' [W /(m K)]	6.4	1.2	6.4	1.2
ρ [kg/m^3]	2500	2800	2500	2800
ρ' [kg/m^3]	2800	2500	2800	
c [J/(kg K)]	640	900	640	900
c' [J/(kg K)]	900	640	900	640
d [m]	3000		3000	
$\partial_z \tau_0$ [°C/km]	50		25	
τ_i [°C]	20 (70)		20 (70)	
$\rho_n Q_{\text{inj}}$ [MT/yr]	0.1		0.36	
t [year]	20	1	20	1.6

2.4. Models tested and practical simulation details

In the results presented in the following section, we have compared the simulation outcomes produced by the following four simplified models against a highly resolved 3D benchmark model that includes overburden and underburden:

COARSE - 3D flow, fully resolved grid in aquifer, 'COARSE' overburden/underburden (cf. Section 2.2).

ADIABATIC - 3D flow, fully resolved grid in aquifer, no overburden or underburden ('ADIABATIC')

VE1 - VE flow model with constant vertical temperature. Fully resolved over/underburden ('FINE').

VE2 - VE flow model with separate temperature for each phase in each vertical column. Fully resolved over/underburden ('FINE').

All models have been implemented using the rapid prototyping abilities of MRST [34], which provides a fully-implicit solver framework based on automatic differentiation. The modeled domain represents a cross-section of the cylindrical domain around the injection well, extending laterally from the well itself and out to the distance at which the cylindrical domain has enough pore space to accommodate twice the amount injected by the end of the simulated period (varies from scenario to scenario). Lateral grid resolution for this part was 100 cells. Moreover, a 20 km additional length was added to the radius of the domain to reduce the impact of the outer grid boundary on the plume development. This additional part of the grid had a very low lateral resolution (20 cells) and is not shown on the plots presented in this article. Vertical grid resolution for over- and underburden was 8 cells in the 'FINE' case, progressively finer towards the aquifer. In the non-VE cases, vertical resolution in the aquifer was 30 cells, progressively finer towards the top. Except for the adiabatic case, a fixed temperature given by the thermal gradient was imposed on the upper and lower boundary. For fluid flow, the inner boundary condition was set to fixed-rate (as determined by the injection rate) and the outer boundary condition to constant-pressure (hydrostatic). The outer boundary condition thus model a fully open aquifer; in this study we limit ourselves to this case, although it is important to note that closed or semi-closed storage formations will have significant boundary effects in terms of pressure buildup.

Fluid properties were modeled as functions of temperature and pressure using full equations of state, based on sampled tables produced using the Coolprop software [35]. A thermal gradient was imposed on all models, except the adiabatic one. The reason for this is that a constant thermal gradient cannot be maintained in an adiabatic model; instead we here used a constant temperature corresponding to the aquifer depth in question.

On the diagrams presented in this section, the outline of the CO_2 plume (black) represents the boundary that separates the zone with more than 0.5 CO_2 saturation from the opposite zone. The line representing the temperature front (red) represents the set of points whose temperature is half-way between initial aquifer temperature and the temperature measured at the injection well. As such, this line should not be confused with the thermal shock described in [15]. We use this line as a measure of the advancement and shape of the thermal perturbation in the aquifer.

We run the simulations using both a 'cold' injection (20°C) and 'hot' injection (70°C) scenario. In the following section we present the result of the 'cold' injections, and note whenever significant qualitative differences were observed when comparing with the corresponding 'hot' injections. It should be noted that even in the 'hot' injection case, the injected CO_2 is still colder than the resident brine when injecting at a depth of 3000 m, even when using the lowest thermal gradient of 25°C/km.

3. Results

3.1. High and low Peclet number

For the examples in this section, we aim to choose parameters that minimize or maximize Pe as a primary consideration and Bl as a secondary consideration. The corresponding parameter values are found in Table 4.

On Figure 5 we compare the simulation outcomes of our models applied on the scenario with highest Peclet number and (as a secondary consideration) highest bleed number, for a 'cold' injection case. On the figure, we can see that the CO_2 plume shapes of all the simplified models match well with the benchmark case, with the exception of a small discrepancy close to the well for the ADIABATIC model. We also note that the advancement of the thermal front is significantly overestimated in the ADIABATIC model and only slightly overestimated in the other ones. The shape of the thermal front is more or less vertical, so it is can be well captured by the VE1 model. Moreover, the thermal front is located behind the advancing CO_2 plume front, and as a consequence there is no difference between the VE1 and VE2 models here. The corresponding 'hot' injection case did not yield any qualitative differences compared to the results of 'cold' injection, and is not shown here for brevity.
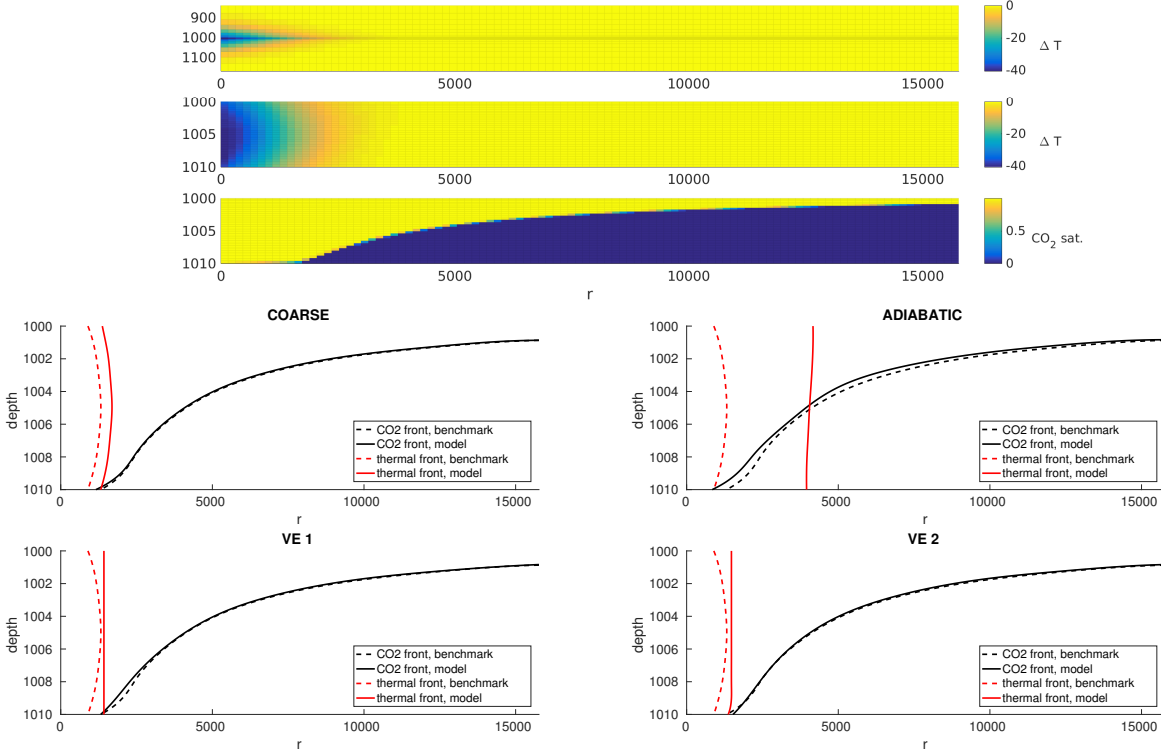
Figure 5: Cold injection, high *Pe* high *Bl* scenario. All plots represent a radial cross-section around the well, with the well at the left side. Upper plot shows the temperature and CO2 profiles in a cross section of the aquifer. The temperature field is shown with and without the overburden in the two upper subplots. The lower four figures compare the benchmark solution with solutions using the simplified models, taken at the last simulation time-step. Broken lines represent the benchmark solution and whole lines the simplified model in question. Red lines represent the shape of the temperature field, black curves that of the CO_2 plume.

On Figure 6, we study the simulation outcomes of our models on the scenario with highest Peclet number and lowest bleed, for the 'cold' injection case (parameters in Table 4). We note that the shape of the thermal zone is notably more complex than in the previous case, and is therefore less well captured by the vertically constant VE1 model. The VE2 model, on the other hand, has a thermal front that to a large extent follows the plume shape, and does a better job here in capturing the shape of the front. If we only consider the lateral position and not the shape of the thermal front, all models do a relatively good job. In terms of CO_2 plume shape, the match is generally very good for all four models, with the exception of a strange bump in the outline produced by the VE1 model. In the 'hot' injection case, this bump disappears (Figure 7). The vertical phase segregation time for both high-Peclet scenarios was estimated to 3 days, using formula (19).

Figure 8 shows the outcomes from simulating the cold injection scenario with lowest Peclet number and highest bleed. This scenario represents injection at a very low rate (0.1 MT/year, which can be considered pilot-scale size), into a very thick aquifer (200 m). Vertical phase segregation for this scenario was estimated to 9.7 years. We see from the upper plot that vertical segregation has not been fully achieved close to the well, which may be explained by the cutoff value for $k_{r,\mathrm{loc}}$ used in (19) as well as the more complex flow patterns in the vicinity of the injection point. Away from the well, both VE models predict the correct plume outline. The plume shapes from the COARSE and ADIABATIC models are both very accurate. The thermal front shape is well captured by the COARSE and the VE1 model, whereas the ADIABATIC model diverges significantly toward the upper and lower boundary, the VE2 model clearly predicts a wrong shape. For the corresponding 'hot' injection scenario, there were no notable qualitative differences in model performance compared to the 'cold' case.

In Figure 9 we see the outcomes from simulating the cold injection scenario with the lowest Peclet number and lowest bleed. The same comments regarding plume shape can be made as in the previous case, but we see that in this case the almost-vertical thermal front is well described by all models except VE2. Estimated vertical segregation time is the same as in the previous scenario, and the simulation time was adjusted upwards accordingly.
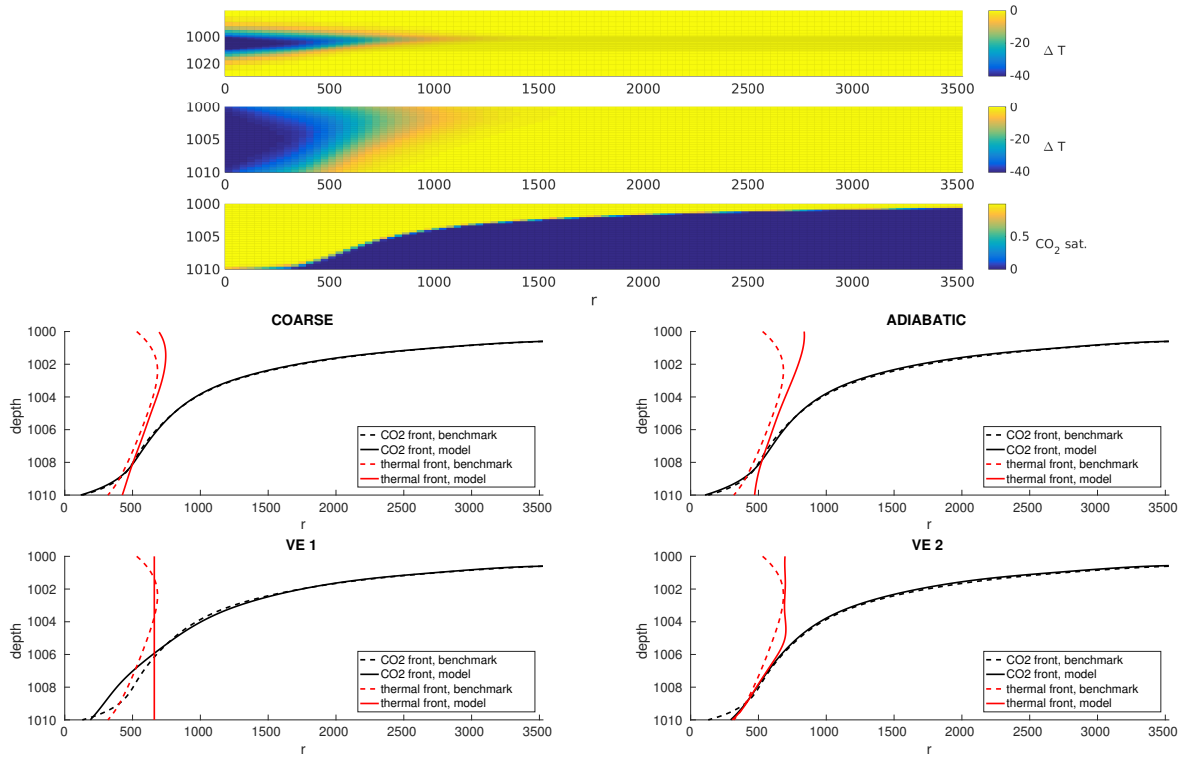
Figure 6: Cold injection, high Pe low Bl scenario. For further explanation, see caption of Figure 5.
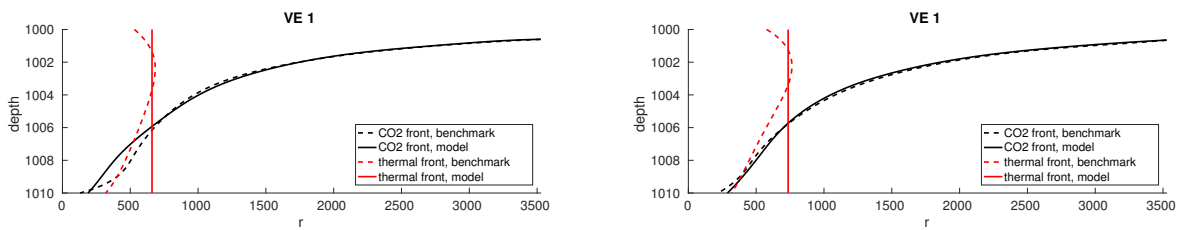

Figure 7: VE1 simulation of High Pe low Bl scenario, comparing 'cold' injection (left) and 'hot' injection (right)
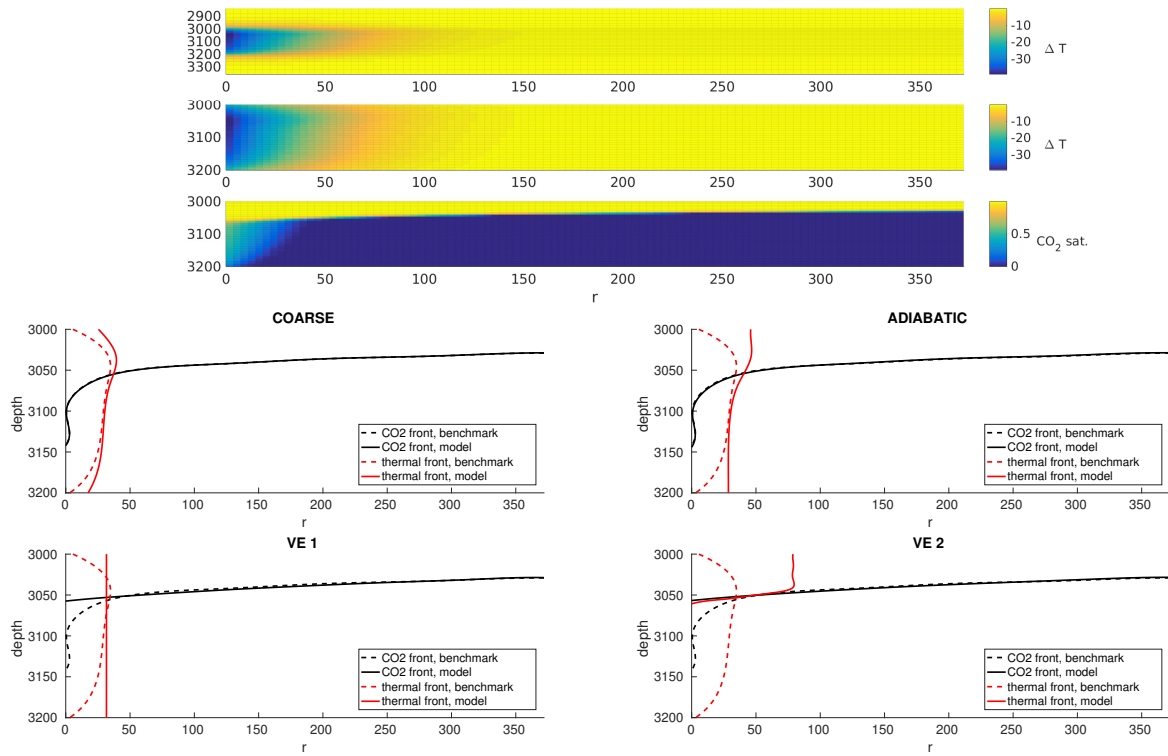
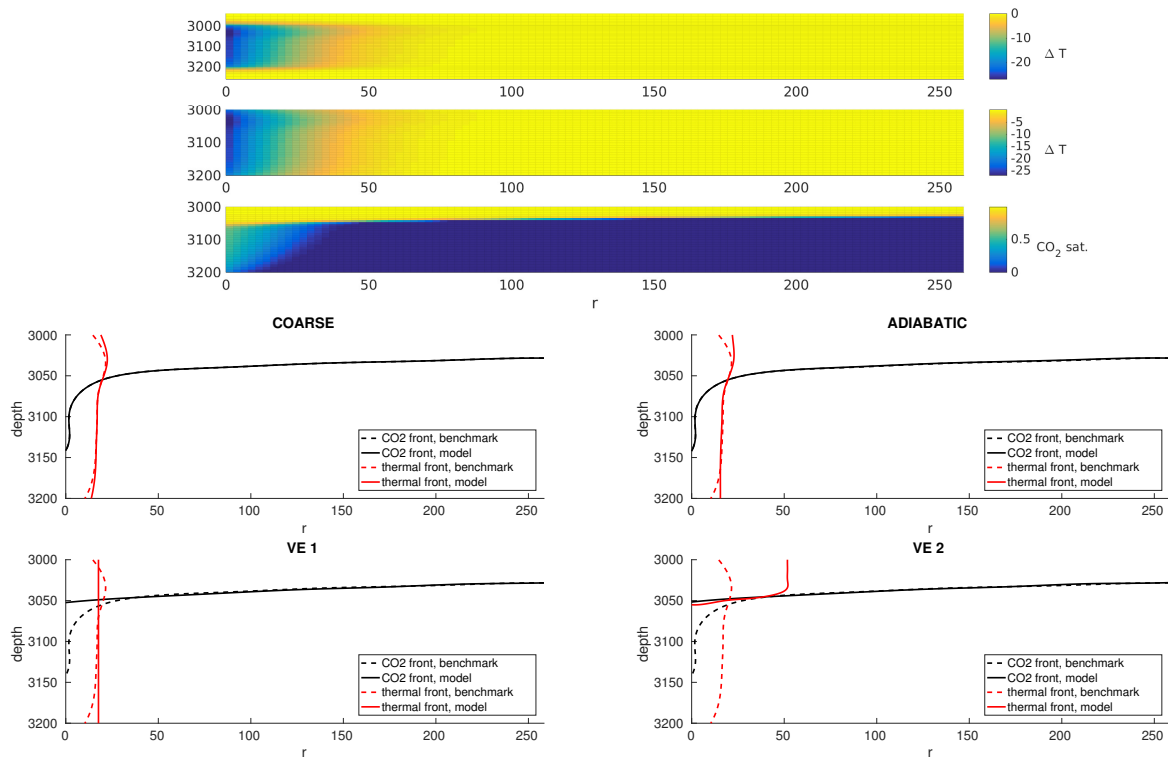Figure 8: Cold injection, low Pe high Bl scenario. For further explanation, see caption of Figure 5.

Figure 9: Cold injection, low Pe low Bl scenario. For further explanation, see caption of Figure 5.
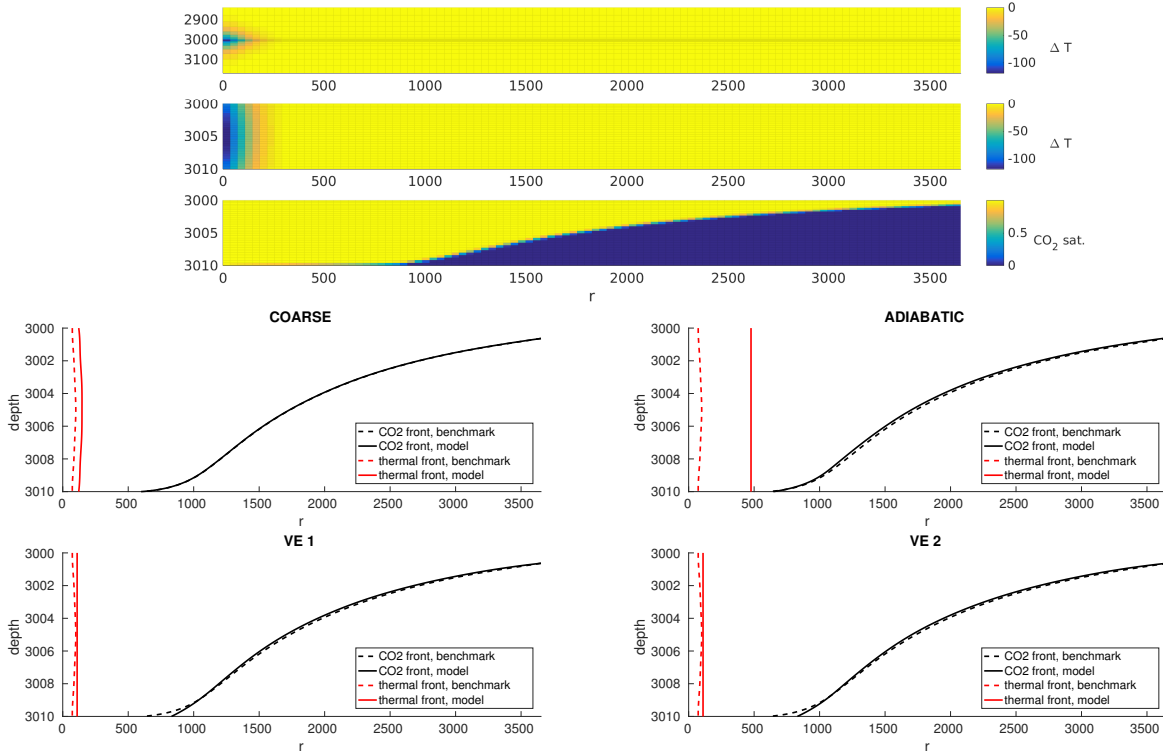
Figure 10: Cold injection, high Bl high Pe (high Bl low Pe is qualitatively similar). For further explanation, see caption of Figure 5.

3.2. High and low thermal bleed

For the examples in this section, we aim to choose parameters that minimize or maximize Bl as a primary consideration and Pe as a secondary consideration. The corresponding parameter values are found in Table 5. As the Bl number depends on almost all the parameters, the only degree of freedom remaining for choosing Pe is the thermal conductivity of the aquifer, λ. In practice, this does not lead to big differences in the simulation outcomes studied, so for brevity we only comment on the outcomes for maximum Pe. In both cases, the estimated vertical segregation time is 180 days. Figure 10 shows the result for the scenario with highest Bl. This is an injection into a thin aquifer with low permeability, and the injection rate has been adjusted down to 0.36 MT/year to avoid unreasonable values for injection pressure. We note that all four models represent plume shape well. The practically vertical front, which remains well behind the CO_2 plume front, is well represented by all models except the adiabatic one, which show a discrepancy in front advancement by several hundred percent compared with the benchmark. The 'hot' injection case does not exhibit any significant qualitative differences from the 'cold' case, and is not presented here.

The scenario with lowest Bl is presented in Figure 11. This is a cold, low-rate injection into a very thick aquifer, and thus have much in common with the case shown in Figure 9, but the permeability is much higher. As a consequence, CO_2 rises directly to the top and spreads out as a thin film, with a estimated vertical segregation time of 16 days. The thermal front, however, is straight and vertical, and well captured by all models except VE2 (which, again, has the tendency to let the thermal front follow the CO_2 front). It is worth noting that compared to the previously described scenarios, the Peclet number is here very low, suggesting that thermal advection plays a comparatively smaller role in this scenario. The corresponding 'hot' injection case is shown in Figure 12. In this case, the injected CO_2 is noticeable hotter than the ambient conditions, and the shape of the thermal front is no longer vertical but significantly skewed towards the top of the aquifer. Only the COARSE model captures this correctly.

3.3. High and low gravity number

We now choose parameters in order to minimize or maximize the gravity number Γ. As a second consideration, we minimize or maximize the bleed number Bl. The corresponding parameter combinations are shown in Table 6.

Figure 13 shows the result from the simulation with the highest Γ and highest Bl. Again, this is a low-rate, cold injection into a highly permeable, thick aquifer, so the CO_2 plume quickly spreads out as a thin film just beneath the caprock and becomes indistinguishable from the top surface on the plots (estimated vertical
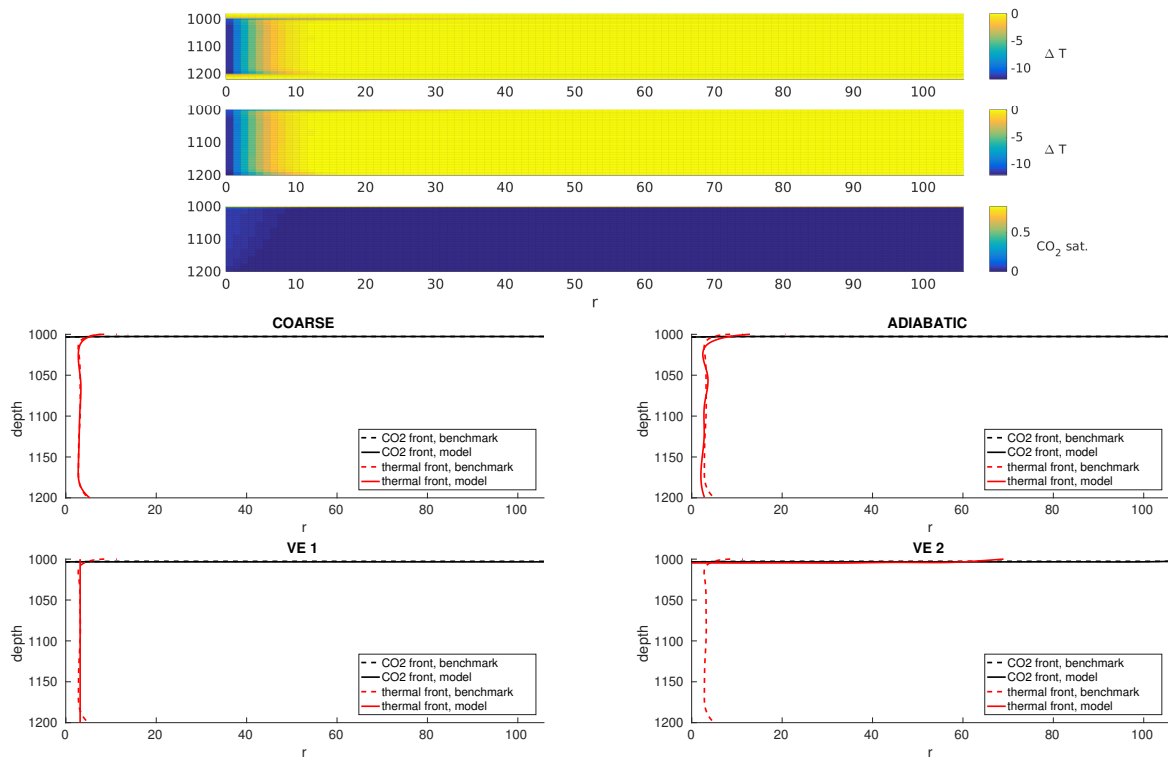
15

Figure 11: Cold injection, low Bl high Pe (low Bl low Pe is qualitatively similar). For further explanation, see caption of Figure 5.
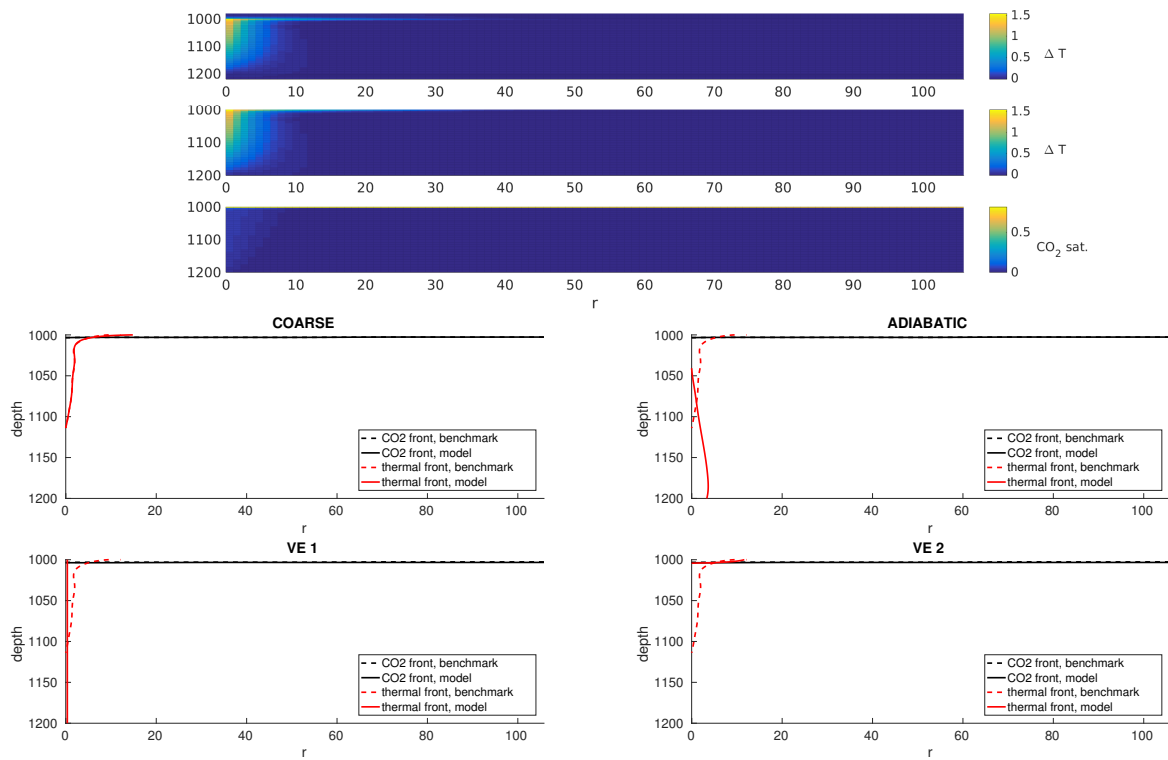

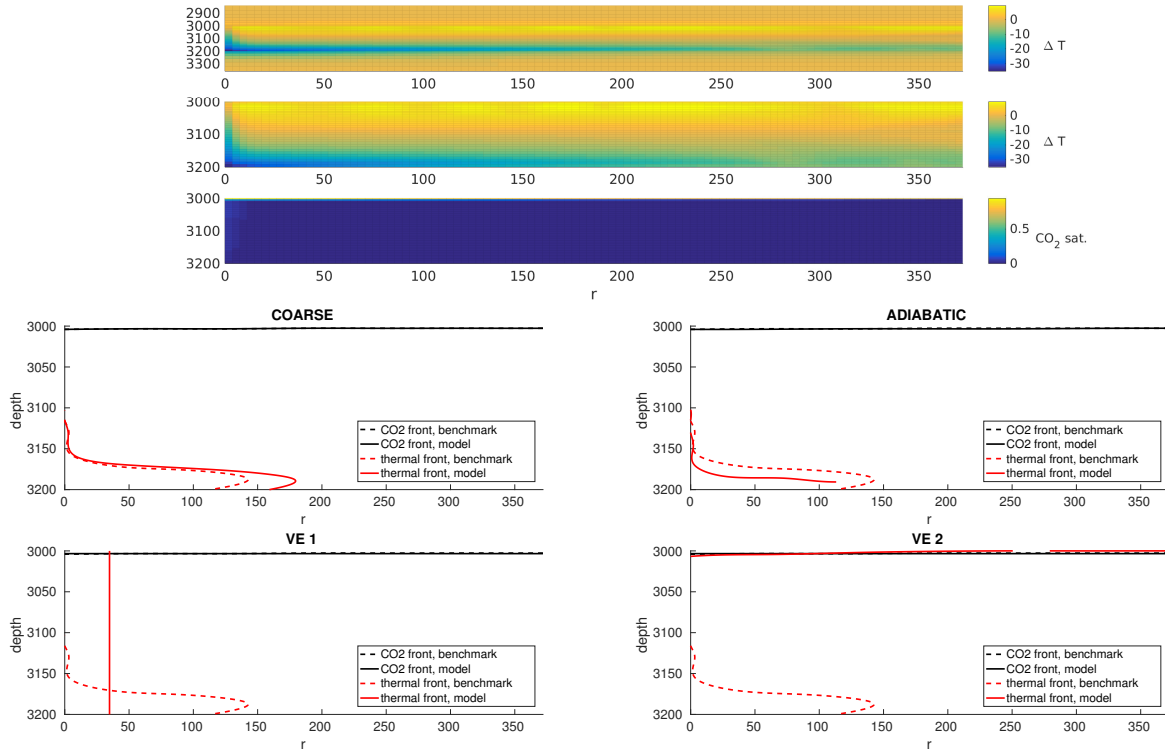Figure 12: Hot injection, low bleed, high Peclet

Figure 13: Cold injection, high Γ high Bl. For further explanation, see caption of Figure 5.

segregation time is 9 days). The shape of the thermal front significantly differ from all other cases studied thus far. What happens is that the rising CO_2 absorbs heat from the surrounding brine, and reaches temperature equilibrium with it even before reaching the top surface. On the other hand, the brine is cooled down in the process, and sinks to the bottom where it becomes the driver of a cold front that creeps outwards along the bottom of the aquifer. This effect is qualitatively captured by the COARSE and ADIABATIC models, but not by the VE models, which are not of much use here. On the upper plot of the thermal field within the aquifer, slight temperature variations can be seen along the whole aquifer extent. These are actually emerging convection cells, driven by the imposed thermal gradient.

The outcome of the simulation with highest Γ and lowest Bl is presented in Figure 14. Qualitatively, the outcome is similar to the previous case, except the absence of thermal convection cells. This may however be due to the fact that the simulation time was only one year (to keep Bl at its lowest), so that the convection cells may not have had sufficient time to develop.

In terms of parameters, the low Γ, high Bl case is identical to the high Bl, high Pe case presented on Figure 10 and discussed in the previous section, so we do not repeat the result here.

Finally, we present the result of the cold injection scenario with lowest Γ and lowest Bl in Figure 15. The thermal front is behind the advancing plume and well captured by all four models. There is however a discrepancy in plume shape between the benchmark and VE models. Estimated vertical segregation time is 1.6 years, which was also the total simulation time. Although the exact explanation for this has not been investigated, it is likely *not* related to the thermal modeling, as fairly accurate thermal fronts are obtained both by VE1 and VE2. For the 'hot' injection cases, no notable qualitative differences were observed and the results thus omitted here.

4. Discussion

As an initial caveat, we should note that even if we have aimed to cover as wide a range of scenarios as possible, the study is far from exhaustive. In particular, the values for Pe, Bl and Γ do not fully characterize a given scenario. It is possible that more differences between hot and cold injections could be observed by focusing the study on the shallower case (where the 'hot' injection scenario would entail injecting CO_2 that is notably hotter than its surroundings). On the other hand, for CO_2 storage purposes, there seems to be a larger interest in cold injection scenarios as these allow for more economical CO_2 storage.
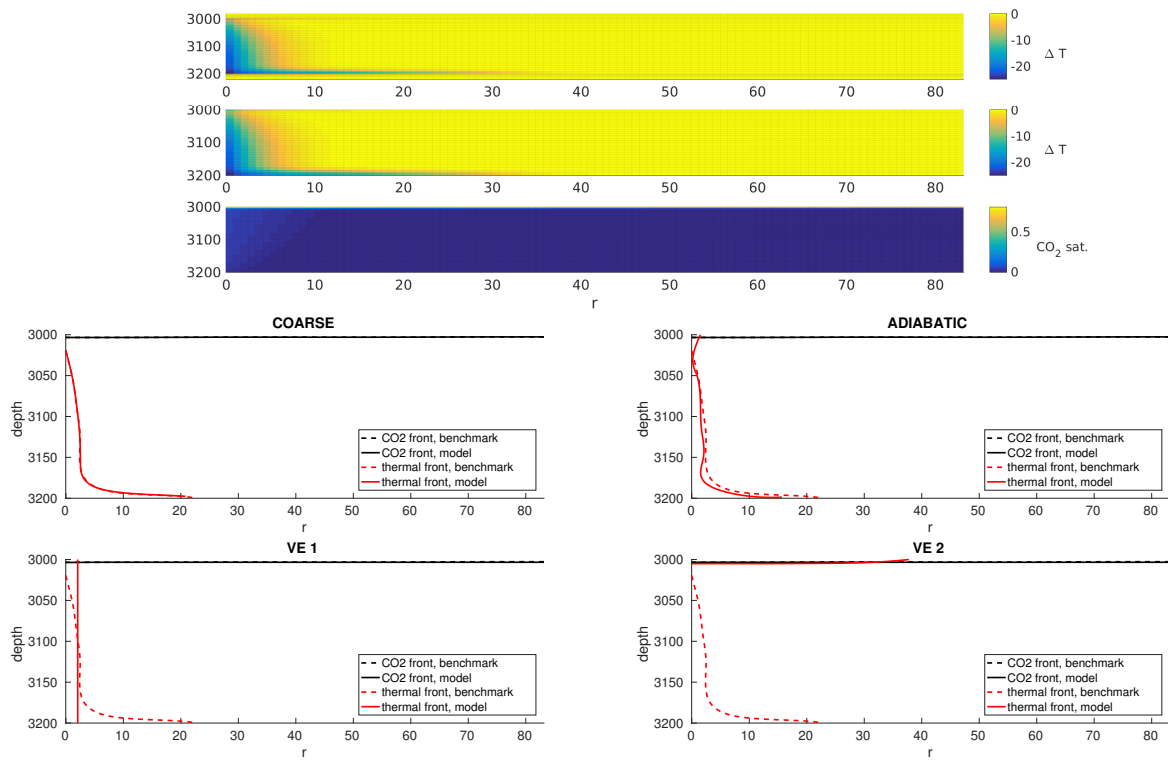
Figure 14: Cold injection, High Γ low Bl. For further explanation, see caption of Figure 5.
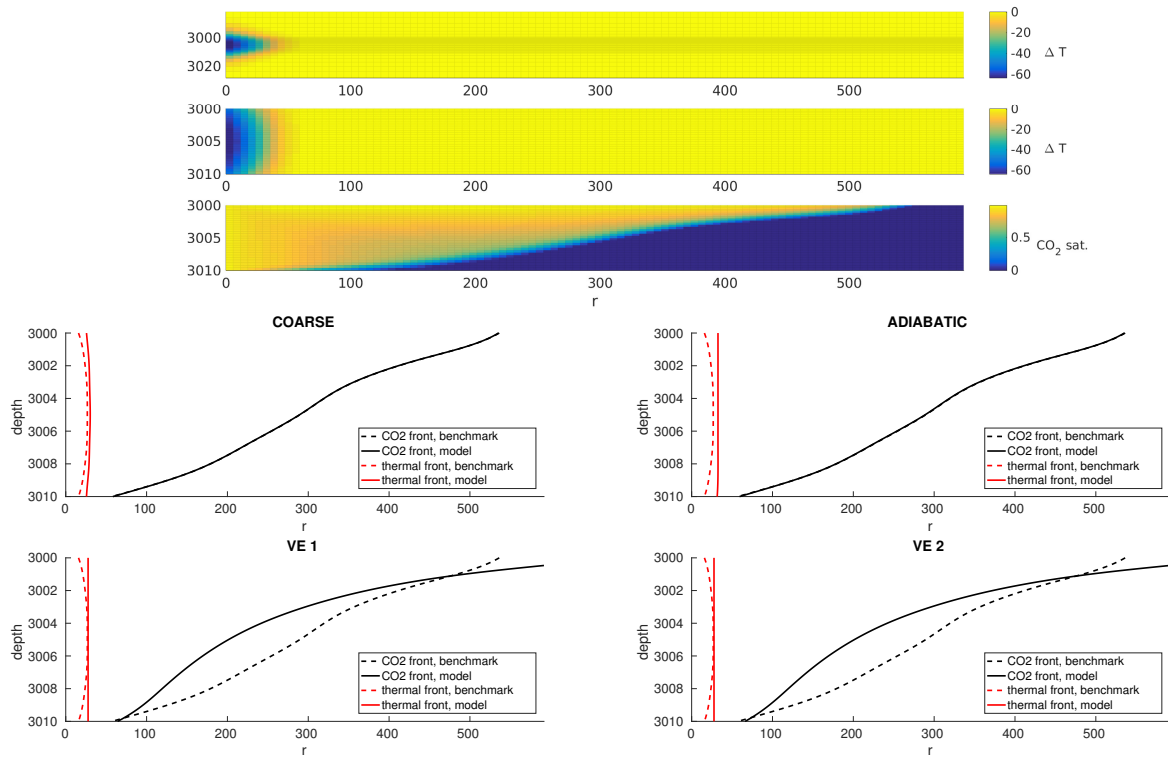

Figure 15: Cold injection, low Γ low Bl. For further explanation, see caption of Figure 5.
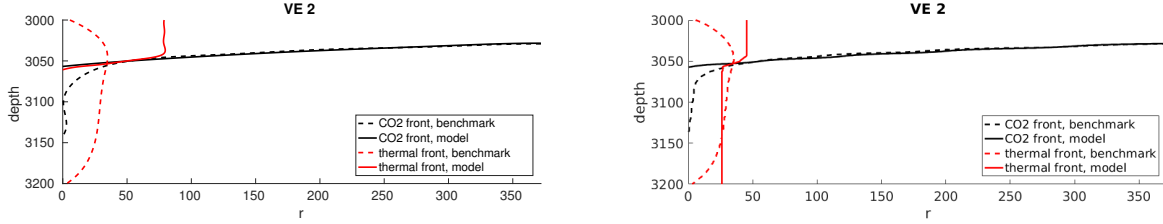
Figure 16: Comparing the result of the VE2 model on the low-Peclet, high-bleed scenario of Section 3 (left) with a modified VE2 model with instant vertical heat transfer in the the single vertical stack of cells closest to the injection point (right).

The examples presented in the previous section all represents extreme cases, and are meant to demonstrate the range of various possibilities that may be encountered, but cannot be fully generalized to delineate trends or provide specific recommendations for arbitrary choices of intermediate parameter values. A choice of thermal model also depends on how much discrepancy can be tolerated. With the possible exception of the cold injection case in Figure 6, errors in thermal front shape or advancement did not translate to significant error in CO_2 plume shape. However, it cannot be concluded that this will always be the case. In particular, many of the examples involved depths of 3000 m, for which even the 'hot' injection scenario represents injection at a temperature lower than the initial aquifer conditions. On the other hand, at 1000 m the injected CO_2 under the 'hot' scenario will be significantly hotter than the surrounding brine, which is likely to cause larger qualitative differences, as exemplified by the contrasting results of Figure 11 and Figure 12. It should also be mentioned that all examples here were carried out under the assumption of a fixed injection rate. In reality, injections may be carried out at a fixed well bottom-hole pressure, for which a stronger dependence of the plume shape on the thermal field is possible. This remains a topic for further study.

Nevertheless, some interesting observations can be made from the results shown. Apart from the high-gravity cases (which are unlikely to be of much practical interest anyway due to the unoptimal use of the aquifer pore space), the shape of the thermal front tends to be either vertical or slightly curved, meaning that the vertically constant temperature profile of the VE1 model often provides a reasonable approximation (depending on the modeler's requirements, of course). The more complex VE2 model is built on the assumption that the heat is carried predominantly by the CO_2 phase inside the plume. From the examples we note that even in the high-Peclet low-bleed scenario, the improvement of the VE2 model over the VE1 one is only modest, and in other situations (e.g. Figure 9) the VE2 thermal profile is clearly not a good approximation. There are two reasons for this. The first is the use of an overly coarse vertical grid (only two cells) to represent heat flow within the aquifer. The effect of this is discussed below in the context of the COARSE model. The other reason is related to the vertical position of the injection point. In all the simulations presented in this paper, the injection point is placed at the bottom of the aquifer. As a consequence, significant heat exchange between CO_2 and brine happens in the vicinity of the wellbore before vertical equilibrium has been established. During its gradual rise from the bottom to the top of the aquifer, the injected CO_2 exchanges heat with its surroundings, including the still-mobile brine. This effect tends to produce a vertical temperature profile and reduces the heat that is carried along laterally with the CO_2 plume. Neither VE model accounts for this effect, but since the VE1 model assumes a vertical profile anyway, the result is often similar to that of the benchmark model. The VE2 model can be modified to emulate this effect by introducing a zone in the aquifer very close to the well with very high ('practically infinite') vertical heat conductivity. On the left plot of Figure 16, we again show the result of applying the VE model on the low-Peclet, high-Bleed scenario from the previous section, and compare it with the result from a modified VE2 model there the heat transmissibility coefficient between the CO_2 and water cell in the vertical pillar closest to the well has been multiplied by a factor of 1000. The corresponding simulation result is shown on the right plot of the figure. It is clear that this result compares much better to the benchmark.

Generally speaking, modeling thermal phenomena using an extended version of a VE flow model requires some specific assumption on the vertical thermal profile. If we do want to improve on the vertically constant profile of the VE1 model, the results above present us with a challenge: the difference between a constant vertical profile and the actual front shape is hard to generalize, and does not seem to follow an analytical description that can be reconstructed column-by-column from upscaled variables. The VE2 model attempts to represent the vertical heat distribution in terms of two regions, but this turns out to be insufficient. A more general approach would be to couple a VE flow model with a fully vertically resolved 3D model for heat flow within the aquifer. The implementation and testing of such a model has however not yet been carried out, to the best of our knowledge.

In terms of the overburden models, the COARSE model tend to slightly over-predict the thermal front

advancement in high-bleed scenarios, while being quite accurate in low-bleed ones. The ADIABATIC model over-predicts even more, and in some cases the over-prediction can be of several hundred percent (Figure 10).

The way the COARSE model underestimates thermal bleed and the VE2 model underestimates diffusion of heat from the CO_2 to the brine phase appears to have a common cause: the computation of heat flow based on an overly coarse grid representation. We recall that in the COARSE model, the overburden is modeled using vertical pillars consisting of a single grid-cell, and for the VE2 model, the CO_2 and brine regions are each represented by vertical pillars with no internal subdivision into cells. The impact this has on the heat transfer rate can be understood through the following argument:

If we again consider the one-dimensional linear diffusion problem with background temperature τ_0 and temperature τ_i imposed at $z = 0$ for time $t > 0$ on the semi-infinite domain $z \in [0, \inf)$, we have:

$$\partial_t \tau - \partial_z(\kappa' \partial_z \tau) = 0$$

with initial and boundary conditions:

$$\tau(z, 0) = \tau_0 \;\; \forall z \in [0, \inf)$$
$$\tau(0, t) = \tau_i \;\; \forall t \in [0, t_{\text{end}}]$$

The analytical solution was already presented in (15), where it was used to estimate L_c. By integrating in time, this means that the heat leaked across the boundary $z = 0$ by time t is proportional to $2(\tau_i - \tau_0)\sqrt{\frac{\kappa' t}{\pi}}$.

On the other hand, if we consider the one-dimensional, finite-volume two-point flux discretized solution for a spatial domain $z \in [0, 2L_c]$, where the domain consists of a *single* cell of length $2L_c = 4\sqrt{t_{\text{end}}\kappa'}$, initially at temperature τ_0 and with an imposed temperature τ_i at its boundary $z = 0$ for time $t > 0$, with the same diffusivity κ', we obtain the following solution:

$$\tau(t) = \tau_0 + (\tau_i - \tau_0)\left[1 - e^{-\frac{t}{8t_{\text{end}}}}\right] \tag{20}$$

Again, by integrating in time, we get that the heat leak across the boundary at $z = 0$ by time t is proportional to $2L_c(\tau_i - \tau_0)\left[1 - e^{-\frac{t}{8t_{\text{end}}}}\right]$. This represents the solution for heat leak into the overburden behind the heat front obtained by the COARSE model, if we consider a fixed injection temperature behind the heat front, and neglect lateral heat flow.

If we compare the analytical and the two-point flux single-cell solution at time $t = t_{\text{end}}$ we have:

  - Heat leaked (analytic) $\sim (\tau_i - \tau_0)\frac{1}{\sqrt{\pi}}L_c \approx 0.56(\tau_i - \tau_0)L_c$

  - Heat leaked (two-point flux) $\sim 2L_c(\tau_i - \tau_0)\left[1 - e^{\frac{1}{8}}\right] \approx 0.24(\tau_i - \tau_0)L_c$

In other words, by the end of simulation t_{end}, the heat leak estimated using an analytic approximation is more than twice the heat leak actually obtained through the two-point flux scheme applied on the single-cell discretization. Moreover, for $t < t_{\text{end}}$, total heat leakage is proportional to the square root of time in the analytical case but approximately linear in the two-point flux solution (thus the COARSE model behaves similarly to the use of a heat loss coefficient, as pointed out in Section 2.2). The lack of an adequate spatial resolution thus leads to significant underestimation and distortion in heat transfer rate from the aquifer into the overburden in the COARSE model, as well as between CO_2 and brine regions in the VE2 model.

5. Conclusions

In this paper we have investigated some simplified approaches to thermal modeling of CO_2 injection scenarios, including models with coarse or no overburden and underburden, and vertical-equilibrium flow models that incorporate conservation of energy under the simplifying assumption of constant vertical temperature, across the whole aquifer thickness or across the thicknesses of each segregated phase.

The models were tested on a set of scenarios that represent widely varying conditions, as measured by the Peclet number, the gravity number and the amount of thermal bleed. The performance of the models vary significantly depending on the scenario under consideration. A coarse representation of the overburden introduces a generally modest error in the position of the thermal front, whereas the absence of an overburden representation (adiabatic model) can lead to a considerable overestimation in thermal front advancement, depending on the amount of thermal bleed. In most cases, the vertical temperature profile can be reasonably well approximated by the VE1 model, which assumes a vertically constant temperature. To be applicable, vertical equilibrium

models require however that phase segregation can be assumed - the time needed for this to happen depends on scenario parameters and can be estimated using (19).

The impact of the over- and underburden on the advancement of the thermal front can often be reasonably approximated by the COARSE model, although it will moderately overestimate the advancement of the front, as discussed in Section 4, especially in high-bleed scenarios. The COARSE model behaves very similar to a linear model based on heat loss coefficients. The ADIABATIC model can be used in some low-bleed scenarios, but can introduce very large errors in situations with high bleed and should be used with caution.

Finally it should be pointed out that vertical equilibrium models are generally intended for large-scale problems and not for detailed studies near the injection well. As such, they are likely not going to be a modeler's first choice for studies limited to the well region. However, the use of VE models that include conservation of energy may be considered a natural extension for larger scale flow modeling problems, whenever the local thermal effects associated with the injection should be included.

Acknowledgments

[1] J. C. Andrew, R. S. Haszeldine, B. Nazarian, The sleipner CO_2 storage site: using a basin model to understand reservoir simulations of plume dynamics, First Break 33 (6) (2015) 61–68.

[2] H. M. Nilsen, S. Krogstad, O. Andersen, R. Allen, K.-A. Lie, Using sensitivities and vertical-equilibrium models for parameter estimation of CO_2 injection models with application to sleipner data, Energy Procedia 114 (2017) 3476 – 3495, 13th International Conference on Greenhouse Gas Control Technologies, GHGT-13, 14-18 November 2016, Lausanne, Switzerland. doi:http://dx.doi.org/10.1016/j.egypro.2017.03.1478.

[3] W. S. Han, G. A. Stillman, M. Lu, C. Lu, B. J. McPherson, E. Park, Evaluation of potential nonisothermal processes and heat transport during co2 sequestration, Journal of Geophysical Research: Solid Earth 115 (B7). doi:10.1029/2009JB006745.

[4] R. Allen, H. M. Nilsen, O. Andersen, K.-A. Lie, Ranking and categorizing large-scale saline aquifer formations based on optimized CO_2 storage potentials and economic factors, International Journal of Greenhouse Gas Control.

[5] G. T. Eigestad, H. K. Dahle, B. Hellevang, F. Riis, W. T. Johansen, E. Øian, Geological modeling and simulation of CO_2 injection in the Johansen formation, Comput. Geosci. 13 (4) (2009) 435–450. doi:10.1007/s10596-009-9153-y.

[6] E. K. Halland, J. Mujezinović, F. Riis (Eds.), CO_2 Storage Atlas: Norwegian Continental Shelf, Norwegian Petroleum Directorate, 2014, npd.no/en/Publications/Reports/Compiled-CO2-atlas.

[7] V. Vilarrasa, O. Silva, J. Carrera, S. Olivella, Liquid CO_2 injection for geological storage in deep saline aquifers, International Journal of Greenhouse Gas Control 14 (2013) 84 – 96. doi:http://dx.doi.org/10.1016/j.ijggc.2013.01.015.

[8] SINTEF ICT, The MATLAB Reservoir Simulation Toolbox: Numerical CO_2 laboratory (Oct. 2014). URL http://www.sintef.no/co2lab

[9] R. Miri, H. Hellevang, Salt precipitation during CO_2 storage - a review, International Journal of Greenhouse Gas Control 51 (2016) 136 – 147. doi:http://dx.doi.org/10.1016/j.ijggc.2016.05.015.

[10] H. Hellevang, V. T. Pham, P. Aagaard, Kinetic modelling of CO_2waterrock interactions, International Journal of Greenhouse Gas Control 15 (2013) 3 – 15. doi:http://dx.doi.org/10.1016/j.ijggc.2013.01.027.

[11] V. Vilarrasa, L. Laloui, Impacts of thermally induced stresses on fracture stability during geological storage of CO_2, Energy Procedia 86 (2016) 411 – 419, the 8th Trondheim Conference on CO2 Capture, Transport and Storage. doi:http://dx.doi.org/10.1016/j.egypro.2016.01.042.

[12] H. A. Lauwerier, The transport of heat in an oil layer caused by the injection of hot fluid, Applied Scientific Research, Section A 5 (2) (1955) 145–150. doi:10.1007/BF03184614.

[13] S. Saeid, F. Barends, An extension of lauweriers solution for heat flow in saturated porous media, in: Proceedings of the COMSOL Conference, Milan, Oct. 2009, COMSOL, 2009.

[14] F. Barends, et al., Complete solution for transient heat transport in porous media, following lauwerier, in: SPE Annual Technical Conference and Exhibition, Society of Petroleum Engineers, 2010.

[15] T. LaForce, J. Ennis-King, L. Paterson, Semi-analytical solutions for nonisothermal fluid injection including heat loss from the reservoir: Part 1. saturation and temperature, Advances in Water Resources 73 (2014) 227 – 241. doi:http://dx.doi.org/10.1016/j.advwatres.2014.08.008.

[16] B. Jie, X. Zhijie, F. Yilin, A coupled thermal-hydro-mechanical simulation for carbon dioxide sequestration, Environmental Geotechnics 3 (5) (2016) 312–324. doi:10.1680/envgeo.14.00002.

[17] S. D. Simone, J. Carrera, B. M. Gmez-Castro, A practical solution to the mechanical perturbations induced by non-isothermal injection into a permeable medium, International Journal of Rock Mechanics and Mining Sciences 91 (Supplement C) (2017) 7 – 17. doi:https://doi.org/10.1016/j.ijrmms.2016.11.001.
URL http://www.sciencedirect.com/science/article/pii/S1365160916303653

[18] D. Settari, Antonin; Walters, Advances in coupled geomechanical and reservoir modeling with applications to reservoir compaction, SPE J. 6. `doi:10.2118/74142-PA`.

[19] M. Preisig, J. H. Prévost, Coupled multi-phase thermo-poromechanical effects. case study: CO_2 injection at In Salah, Algeria, International Journal of Greenhouse Gas Control 5 (4) (2011) 1055–1064.

[20] B. N. Nguyen, Z. Hou, M. L. Stewart, C. J. Murray, A. Bonneville, Thermal impact of {CO2} injection on geomechanical response at the futuregen 2.0 site: A three-dimensional thermo-geomechanical approach, International Journal of Greenhouse Gas Control 54, Part 1 (2016) 29 – 49. `doi:https://doi.org/10.1016/j.ijggc.2016.08.026`.

[21] V. Vilarrasa, J. Rutqvist, Thermal effects on geologic carbon storage, Earth-Science Reviews 165 (2017) 245 – 256. `doi:https://doi.org/10.1016/j.earscirev.2016.12.011`.

[22] J. M. Nordbotten, M. A. Celia, Geological Storage of CO_2: Modeling Approaches for Large-Scale Simulation, John Wiley & Sons, Hoboken, New Jersey, 2012.

[23] I. S. Ligaarden, H. M. Nilsen, Numerical aspects of using vertical equilibrium models for simulating CO_2 sequestration, in: Proceedings of ECMOR XII–12th European Conference on the Mathematics of Oil Recovery, EAGE, Oxford, UK, 2010.

[24] K.-A. Lie, H. M. Nilsen, O. Andersen, O. Møyner, A simulation workflow for large-scale CO2 storage in the Norwegian North Sea, Comput. Geosci. 20 (3) (2016) 607–622. `doi:10.1007/s10596-015-9487-6`.

[25] H. M. Nilsen, K.-A. Lie, O. Andersen, Analysis of CO2 trapping capacities and long-term migration for geological formations in the Norwegian North Sea using MRST-co2lab, Computers & Geosciences 79 (2015) 15–26. `doi:10.1016/j.cageo.2015.03.001`.

[26] S. Gasda, W. Gray, H. Dahle, Vertically integrated models with coupled thermal processes, European Association of Geoscientists and Engineers, EAGE, 2014.

[27] H. M. Nilsen, K.-A. Lie, O. Andersen, Robust simulation of sharp-interface models for fast estimation of CO2 trapping capacity, Comput. Geosci. 20 (1) (2016) 93–113. `doi:10.1007/s10596-015-9549-9`.

[28] O. Andersen, S. Gasda, H. Nilsen, Vertically averaged equations with variable density for CO_2 flow in porous media, Transp. Porous Media (2014) 1–33`doi:10.1007/s11242-014-0427-z`.

[29] K.-A. Lie, An Introduction to Reservoir Simulation Using MATLAB: User guide for the Matlab Reservoir Simulation Toolbox (MRST), SINTEF ICT, `http://www.sintef.no/Projectweb/MRST/publications`, 2nd Edition (December 2015).

[30] T. LaForce, J. Ennis-King, L. Paterson, Magnitude and duration of temperature changes in geological storage of carbon dioxide, Energy Procedia 37 (2013) 4465 – 4472, gHGT-11 Proceedings of the 11th International Conference on Greenhouse Gas Control Technologies, 18-22 November 2012, Kyoto, Japan. `doi:http://dx.doi.org/10.1016/j.egypro.2013.06.351`.

[31] J. M. Nordbotten, M. A. Celia, Similarity solutions for fluid injection into confined aquifers, J. Fluid Mech. 561 (2006) 307–327. `doi:10.1017/S0022112006000802`.

[32] B. Court, K. W. Bandilla, M. A. Celia, A. Janzen, M. Dobossy, J. M. Nordbotten, Applicability of vertical-equilibrium and sharp-interface assumptions in CO2 sequestration modeling, International Journal of Greenhouse Gas Control 10 (2012) 134–147. `doi:10.1016/j.ijggc.2012.04.015`.

[33] J. M. Nordbotten, H. K. Dahle, Impact of the capillary fringe in vertically integrated models for CO_2 storage, Water Resources Research 47 (2). `doi:10.1029/2009WR008958`.
URL `10.1029/2009WR008958`

[34] The MATLAB Reservoir Simulation Toolbox, version 2016a (7 2016).
URL `http://www.sintef.no/MRST/`

[35] I. H. Bell, J. Wronski, S. Quoilin, V. Lemort, Pure and Pseudo-pure Fluid Thermophysical Property Evaluation and the Open-Source Thermophysical Property Library CoolProp, Ind. Eng. Chem. Res. 53 (6) (2014) 2498–2508. `doi:10.1021/ie4033999`.